

# Shower centre determination in a high granularity digital sampling calorimeter<sup>\*</sup>

WANG Hong-Kai<sup>1</sup> WANG Liang<sup>1</sup> HAN Jing-Ru<sup>1</sup> ZHAO Chuan-qi<sup>1</sup>  
 ZUO Jia-Xu<sup>1</sup> ZHANG Chun-Hui<sup>2;1)</sup>

<sup>1</sup> Nuclear and Radiation Safety Center, Ministry of Ecology and Environment, Beijing, 100082, China

<sup>2</sup> Shenzhen Institutes of Advanced Technology, Chinese Academy of Sciences, Shenzhen, 518055, China

**Abstract:** The precise measurement of photon or electron impact position is the prerequisite to reconstruct the origin of two photons events from decay of  $\pi^0$  and  $\eta$  mesons or the di-electron channel from quarkonia decay. To facilitate such a measurement, an electromagnetic calorimeter prototype using Monolithic Active Pixel Sensors (MAPS) was built and tested. The  $30 \times 30 \mu\text{m}^2$  granularity coupled with an optimized centre of gravity with power law weight method dedicatedly developed for the particle counting digital calorimeter, makes precise reconstruction of impact position of electromagnetic showers to be straightforward. Parameters of the method are optimized and the performance is verified with the GEANT based simulation and the experimental data which were collected at DESY and CERN SPS. The accuracy of the reconstruction of electron or photon impact position can be better than  $30 \mu\text{m}$  in a broad range of energies.

**Key words:** calorimeter, electromagnetic shower, Monte-Carlo simulation, shower central position, spatial resolution

**PACS:** 29.40.Vj

## 1 Introduction

One of the aims of modern particle physics is to allow us to experimentally verify predictions of fundamental structures and states of substances in the early universe. With the world's largest and most powerful collider, the Large Hadron Collider (LHC), it is possible to accelerate heavy ions to several TeV per nucleon in the centre of mass system, which helps to transform the quarks and gluons into a new state called Quark Gluon Plasma (QGP) [1]. As the dedicated detector at LHC, ALICE [2] is studying this form of matter that exists shortly after the Big Bang.

As a clean hard probe of QGP, direct photons in the forward region yield the crucial information about the initial state parton distributions in the colliding system, and is therefore sensitive to effects of gluon saturation [3–6], nevertheless significant background from decay photons of  $\pi^0$  blurs the measurement results. Heavy quarks (charm and bottom) could also serve as a probe [7, 8] of parton distribution because they are created only in the hard processes that occur during initial scatterings and the suppression of forward quarkonium production is observed by ALICE recently [9]. However, the possibility of final state modifications [10] in the collision system may make final conclusion from such a measurement to be difficult.

To facilitate the understanding of these open questions stated previously, it is usually required to enhance the selection of direct photons by rejecting the two decay photons from  $\pi^0$ ,  $\eta$ -mesons or the di-electron from quarkonium at forward rapidity when their invariant mass are reconstructed. However, due to the longitudinal boost, the separation between the photons decreases with increasing energy and rapidity to the point that the two decay photon showers can no longer be resolved, after which the two decay photons are indistinguishable from a single photon since they are merged. It is obviously necessary to require calorimeter with the capability to identify the showers at a distance of few mm. Moreover, isolation cuts must be employed at high transverse momenta when the decay photons can no longer be resolved and identified efficiently. Such a separation power requires precise shower centre reconstruction and it can only be fulfilled with a fine granularity compact sampling electromagnetic calorimeter with longitudinal segmentation.

Forward Calorimeter (FoCal), which is proposed to discriminate the two photons with small angle at large distance from the interaction point in ALICE [5], employs CMOS based Monolithic Active Pixel Sensors (MAPS) [11, 12] with  $\mu\text{m}$  level granularity. Such a high granularity will further not only provide a precise measurements of  $\pi^0$  productions up to large momenta

<sup>\*</sup> Supported by National Natural Science Foundation of China (No. 11505076)

1) E-mail: ch.zhang@siat.ac.cn

$p_T > 20$  GeV/ $c$ , which are the dominant background of the direct photon measurements, but also allows to reject decay photons directly.

There are several formulas have been proposed and compared to determine the shower centre position [13–15]. Most of them were based on the energy deposition of electrons (or photons) in laterally segmented calorimeters. The centre of gravity method is one of the most common formula to reconstruct the shower centre in a conventional sampling calorimeter. It sums the number of blocks in the shower cluster and assigns a weight factor depending of the energy. This is inapplicable for a digital calorimeter because only digital signals can be provided by the pixel response (0 or 1). In comparison to the simplest linear weighting case, an optimized weight method with power weight applied to the density defined as the sum of the hits in a pixel region is established and addressed based on simulated and experimental data. This method enhances the significance of the core region of the shower. By confining the density for all properly working sensors, the bias from the wide tail of the electromagnetic shower can be suppressed.

## 2 Experiment and Simulation Setup

### 2.1 Calorimeter Prototype

In order to facilitate the design of the high granularity layers for the proposed FoCal upgrade, a prototype with full MAPS sensors has been manufactured in Utrecht University, the Netherlands [16]. The small Molière radius ( $R_M \approx 10$  mm) and radiation length of tungsten allow the FoCal prototype to be compact in both the transverse and longitudinal directions. The thickness of each layer is 4 mm, of which 3 mm is tungsten and the thickness is approximately equals to  $0.97 X_0$ . A tungsten block with 20 mm thickness is located just behind  $20 X_0$ , resulting in  $\approx 28 X_0$  in total in the longitudinal direction of the detector. In the transverse direction, the size of the active area for every layer is approximately  $4 \times 4$  cm<sup>2</sup>. Two identical modules, each with two sensors, are mounted in alternating orientations, with the sensors covering opposite halves of the detector and facing each other (Fig. 1). This design leads to a narrow gap ( $\approx 0.1$  mm) between sensors along the  $x$  direction and an overlap ( $\approx 0.1$  mm) along the  $y$  direction in each layer. The size of each sensor is  $1.92 \times 1.92$  cm<sup>2</sup>, and  $640 \times 640$  pixels are integrated in this area. In total, there are 96 PHASE2/MIMOSA-23 [17] sensors with three different types of thickness and resistivity of the epitaxial layer in the calorimeter prototype. Due to the large number of pixels in every sensor, a dedicated PCB was made to read out the data generated in the sensor. The PCB of

the sensor is connected to the readout board via a flat cable.

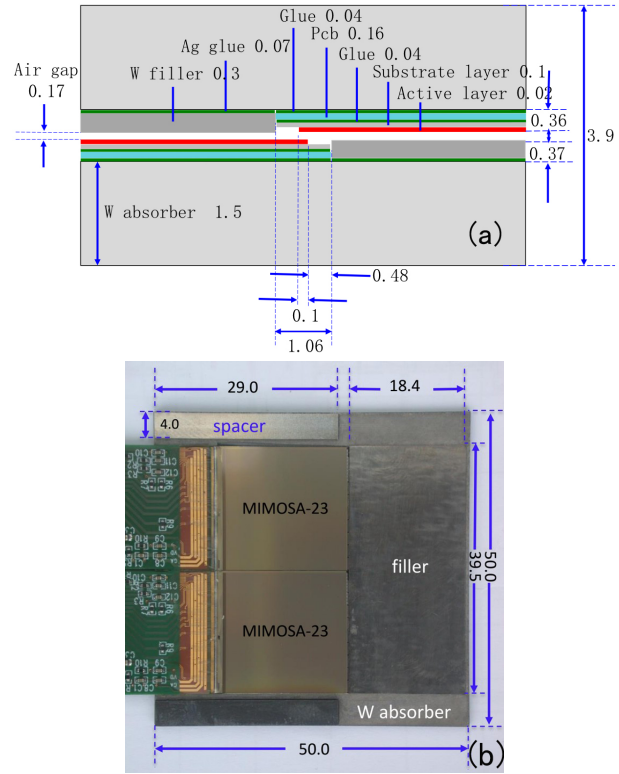


Fig. 1. (a) The structure of layer components, the unit of the values is mm. (b) An image of a full module.

Some sensors, channels and pixels are malfunctioning during manufacturing and assembly. These regions together with the noise pixels which are activated when there are no particles in the detector amount to an insensitive fraction approximately 16.7% of the total sensor area installed in the calorimeter.

### 2.2 Simulation

The geometry of the calorimeter has been constructed in detail in a GEANT4-based\* simulation platform. Instead of implementing different thickness of epitaxial layers, the  $20 \mu\text{m}$  thick epitaxial layer were applied for all the sensors in the detector. The energy depositions of particles in the sensitive layers of the silicon sensors for all individual pixels can be recorded. In addition, charge diffusion is modelled by redistributing the equivalent charge to the energy deposition over several adjacent pixels by introducing parameters which describe charge attenuation and diffusion. The details of tuning the model can be referred to [19].

\*GEANT4 version 10.00.p01 with emStandard physicslist[18]

### 2.3 Data collection and event selection

Several beam measurements have been carried out in the past few years. Two of them, which concentrate on the electrons, are used in the present work. The experimental setup using CERN SPS high energy electron beam is shown in Fig. 2. The momentum range covers from 30 to 244 GeV/c. Several scintillators are designed and placed in the front and rear sides of the calorimeter to provide not only the external triggers but also the beam position selection information for the data acquisition system. The electrons with lower momentum (5.4 GeV/c) was obtained at DESY in Germany, and the setup had the similar layout as SPS setup.

A position cut of the cluster on the first layer (layer 0) in order to get rid of the geometry effects such as the edge, gap and overlap. The showers, with cluster on layer 0 that are close to the edge ( $|x| \geq 15$  mm and  $|y| \geq 15$  mm) and the gap area ( $|y| \leq 1.5$  mm), are not involved in the analysis. In addition, the double count effect happens in the overlap region ( $|x| \leq 3$  mm) could deteriorate the accuracy of shower centre reconstruction and thus those events should also be rejected. The data that collected during the beam measurements and involved in the analysis in this paper is summarized in Tab.1.

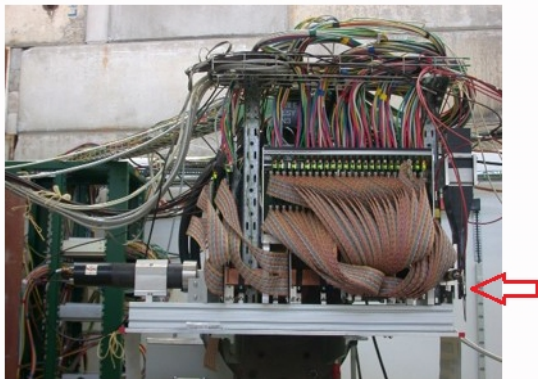


Fig. 2. The side view of the experimental setup at CERN SPS. The calorimeter stack is surrounded by the flat cables. The red arrow indicates the beam direction towards the front side of the calorimeter.

Table 1. The properties and statistics of the different data samples collected in the test beams.

Site	Particle type	$p$ (GeV/c)	$N_{events}$
DESY T22	$e^+$	5.4	4984
CERN SPS H8	$e^+$	30	10539
CERN SPS H8	$e^+$	50	7535
CERN SPS H8	$e^+$	100	10853
CERN SPS H8	$e^-$	244	1920

The simulated setup is uniformly irradiated at 5 different energies by a  $15 \times 15$  mm<sup>2</sup> mono-energetic parallel electron beam impinging on the front surface of the calorimeter. The same geometry cuts as experimental data were also applied to select the events.

Table 2. The statistics of data samples in the simulation.

$p$ (GeV/c)	Particle type	$N_{events}$
5.4	$e^-$	1213
30	$e^-$	2082
50	$e^-$	2015
100	$e^-$	2076
244	$e^-$	2085

## 3 Shower centre reconstruction method

### 3.1 Coordinate system and sensor alignment

Fig. 3 shows the coordinates system, the quadrant numbers and the layer numbers definition in the analysis. The ideal coordinates of a given pixel are acquired by using the information of line and column numbers which represent the relative position in the sensor. Note that the misalignment from assembly process, gap and overlap are not taken into account in this calculation.

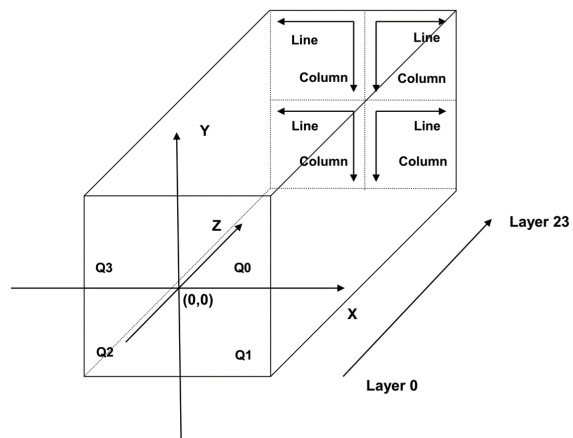


Fig. 3. The definition of coordinate system, quadrant, and layer number in the calorimeter.

The construction of the prototype allows positioning deviations of the sensors within the  $x$ - $y$ -plane. The task of the alignment is to correct these. To increase the connections between the sensors in the calorimeter, tracks which penetrate different quadrants are preferred and thus combs muons are used. The possible errors can be described by a rotation angle  $\theta$  about the  $z$  axis and a displacement of the sensor as a translation in  $x$  and  $y$  directions. The transformation between the ideal coordinates  $\vec{C}^i(x^i, y^i, z^i, 1)$  and the aligned coordinates  $\vec{C}^a(x^a, y^a, z, 1)$  can be described by:

$$\vec{C}^a = T_{xyz}(\Delta x, \Delta y, \Delta z) \cdot R_Z(\theta) \cdot \vec{C}^i \quad (1)$$

Here  $T_{xyz}(\Delta x, \Delta y, \Delta z)$  is the translate matrix and  $R_Z(\theta)$  represents the rotation matrix along the  $z$ -axis. Since the position of layer along  $z$  direction is mechanically restrained, the nominal value of  $z$  for every layer is assumed ( $\Delta z = 0$ ). It therefore leaves 3 parameters  $\vec{\alpha}(\Delta x, \Delta y, \theta)$  for every sensor to be determined by:

$$\arg \min \chi^2 = \arg \min \left( \frac{\sum_{i=1}^n (\vec{C}_i^a(\vec{\alpha}) - \vec{C}_i^{fit}(\vec{\alpha}))^2}{n\sigma^2} \right) \quad (2)$$

Here  $n$  is the number of hits and  $\sigma$  is the standard deviation associated to the reconstructed tracks. When track-based alignment is performed on many tracks, the  $\chi^2$  becomes a function of the alignment parameters, and it has a minimum value corresponding to the true detector geometry which can be reached through iteration. Since the accurate positions of pixels in the simulation can be obtained, thus, it is not necessary to align the detector in the simulation.

In order to prevent the detector deformations that leave the minimization results unchanged by biasing the reconstructed track parameters. Two sensors located in the first layer and last layer are fixed as references. All in all, with the procedures stated above, the accuracy of alignment for the experimental data can be better than  $5 \mu\text{m}$  [16].

### 3.2 Shower centre position determination

The method of shower centre reconstruction can be used for both electrons and photons. Different from the conventional energy measurement calorimeter, the pixel in a digital calorimeter can only provide binary response, therefore, an estimation of a shower centre would make use of properly working sensors in all the layers except the first layer.

Considering the calculation speed and precision, several optimization steps are developed for this method. One can find the coarse shower centre according to the position of the bin with highest amplitude of a summed pixel response transverse hit profile derived from all the layers (Fig. 4), and the corresponding quadrant where the shower is located can be identified. In order to reduce the bias may be introduced by the inhomogeneous of the transverse hit profile, all the hits from all the good layers in the same quadrant are used in the further calculation. A squared region  $[p, p]$  which covers the shower core region can be set once the coarse centre is determined. The value of  $p$  is obtained according to the Molière radius ( $\approx 1 \text{ mm}$ ) of the calorimeter because it contains the majority active pixels for a given shower. Instead of measuring the energy deposition, the density  $A_{l,c}$  of the hits with line and column  $\{l, c\}$  for all layers can be calculated as:

$$A_{l,c} = \sum_{L=1}^{23} h(l, c, L), \quad \{l, c\} \in [p, p] \quad (3)$$

where  $h$  is the response in the corresponding pixel in a given layer  $L$ .

In comparison to the simplest linear weighting case, an optimized power weight is applied. It enhances the significance of the core region of the shower. By setting a cut on the density for all properly working sensors, the bias from the wide tail of the electromagnetic shower can be suppressed. In this method the weight  $\omega_i$  is given by

$$\omega_{l,c} = \max\{0, A_{l,c} - W_0\} \quad (4)$$

Here  $W_0$  is a dimensionless parameter providing a threshold for the density. Consequently, only the pixel regions having the density higher than  $W_0$  are taken into account for calculating the shower centre. Then the position for the shower centre is:

$$(x_0, y_0) = \frac{\sum_{\{l,c\} \in [p,p]} \omega_{l,c}^t \cdot (x^a\{l,c\}, y^a\{l,c\})}{\sum_{\{l,c\} \in [p,p]} \omega_{l,c}^t} \quad (5)$$

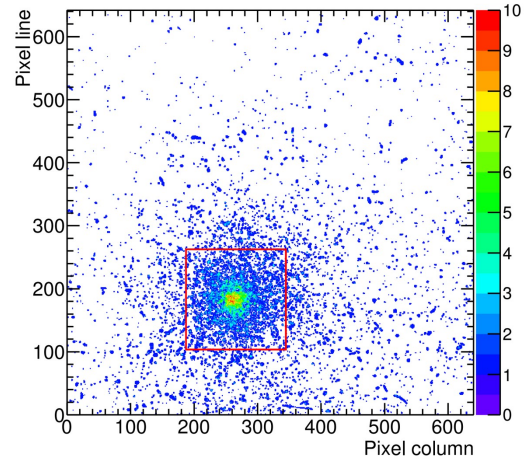


Fig. 4. The transverse hit profile for an electron shower event ( $244 \text{ GeV}/c$ ) in the experiment, and the region of the profile with pixels bin contents above  $W_0 = 3$  is marked with a red squared box.

### 3.3 Cluster on the first layer

To experimentally verify the precision of this method, electrons are used because they are charged particles that can leave a group of active pixel hits which called a cluster in the first layer. The cluster can be treated as an estimate of incident electrons and the its precision can be verified in the simulation since the primary positions of electrons are available. Fig. 5 shows the accuracy of using centre of cluster as true electron impact position in the simulation. The two peaks sit at  $\pm 15 \mu\text{m}$  indicate the ideal coordinate definition of pixels (the distance from a

pixel centre to the edge is  $15 \mu\text{m}$ ). The cluster in the first layer is identified within the range of 1 mm from the reconstructed shower centre. As can be interpolated from Tab.(3), the noise hits in the cluster search radius are less than 0.3 pixel/event and 0.03 pixel/event for  $10^{-4}$  and  $10^{-5}$  pixel noise probability, respectively. It is significantly lower than the average number of hits in a signal cluster [16]. Once the cluster is identified, its gravity centre  $(x_c, y_c)$  can be determined as the shower impact reference position. Photons behave similarly to electrons in the electromagnetic calorimeter although they are uncharged, the shower centre reconstruction method is nevertheless valid.

Table 3. Noise probability of each pixel for layer 0 of different data samples.

Data source	Noise level	Momentum (GeV/c)
experiment	$10^{-5}$	5.4, 244
experiment	$10^{-4}$	30, 50, 100
simulation	$10^{-5}$	5.4, 30, 50, 100, 244

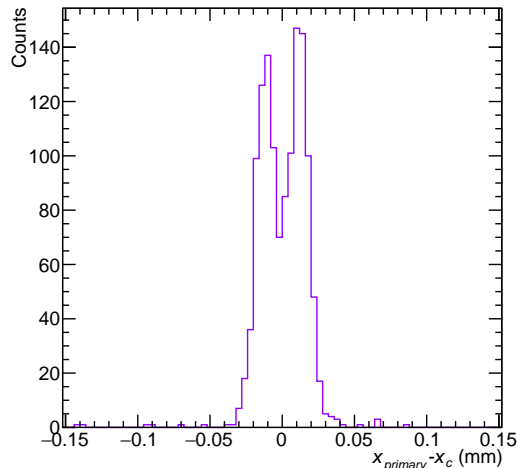


Fig. 5. Distribution of the residual between primary electron (100 GeV/c) position and cluster centre position in the first layer in the simulation.

## 4 Parameter optimization

### 4.1 Optimization for threshold $W_0$

$W_0$  allows to set a threshold to calculate the density in the pixel region, especially when the energy of electrons decreases due to low hit count. High  $W_0$  favours the shower core region but decreases the number of pixel regions used in the calculation and leads to a higher probability of reconstruction failures, while small  $W_0$  has the drawback that may bias the centre calculation due to the large number of low density pixel regions. This effect is directly relevant to the efficiency of shower centre reconstruction. The reconstruction efficiency is defined as

the number of electrons which the centre are successfully reconstructed, divided by the total number of electrons with clusters in layer 0. The reconstruction efficiency as various  $W_0$  is shown in Fig. 6, the reconstruction efficiency at different  $W_0$  is related to the energy of electrons. Higher  $W_0$  refines the calculated area but reduces the efficiency dramatically, and this decrease happens for lower threshold value when the electron energy is decreasing. Therefore, it is desirable to maintain the efficiency at a relative high level by selecting the appropriate  $W_0$  value at different momentum.

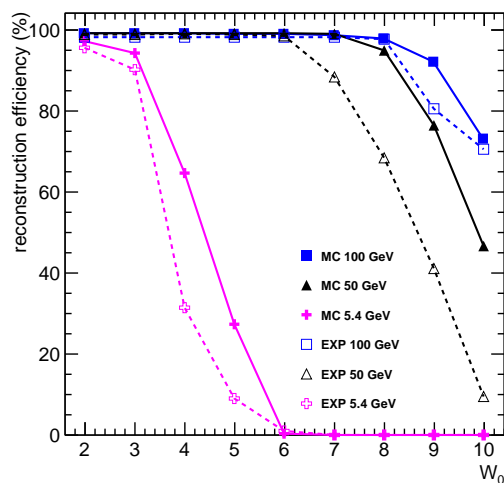


Fig. 6. Shower centre reconstruction efficiency at 3 energies as a function of threshold parameter  $W_0$  in the simulation and experiment.

The shower centre reconstruction accuracy is also sensitive to the  $W_0$  selection since the radius around the centre influence the result. Fig. 7 indicates the reconstruction accuracy as a function of  $W_0$ . The accuracy  $\sigma_{x_0-x_c}$  is defined as the width of the distribution by comparing the reconstructed shower centre and the cluster centre position which is identified in the first layer. The data points are selected at relative high reconstruction efficiency ( $> 95\%$  for 30, 50, 100, and 244 GeV/c,  $> 90\%$  for 5.4 GeV/c). It is obvious that the accuracy becomes better at certain range of  $W_0$  and tends to be stable at moderate  $W_0$ . The accuracy is no longer keep decreasing at higher  $W_0$  due to the fact that shower core region shrinks excessively and introduces significant fluctuations for shower centre calculations by this method. For demonstrating results in the later section, it requires to reach a compromise between reconstruction efficiency and accuracy by select different  $W_0$  values according to the beam momentum. The  $W_0$  values that will be used to show the final results can be summarised in Tab. (4).

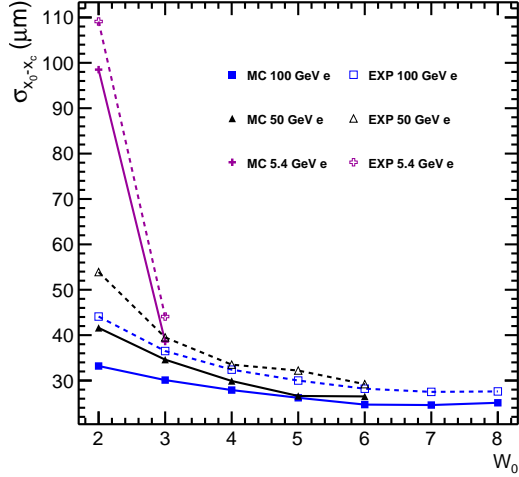


Fig. 7. Shower centre reconstruction accuracy as a function of threshold  $W_0$  ( $t=2$ ) for experimental and simulated electrons with momenta of 5.4, 50 and 100 GeV/c. Note that the data points are selected at relative high reconstruction efficiency for different energies.

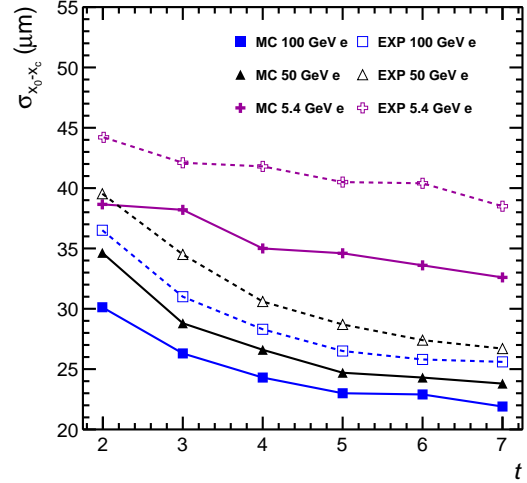


Fig. 8. Shower centre reconstruction accuracy as a function of power index  $t$  ( $W_0=3$ ) for experimental and simulated electrons with 3 different energies.

Table 4. Optimized  $W_0$  values for different energies.

Momentum (GeV/c)	$W_0$
5.4	3
30	4
50	5
100	7
244	9

## 4.2 Optimization for power index $t$

The other parameter  $t$ , which is the power index to enhance the shower core region of a given shower, can also be optimized through checking the reconstruction accuracy. Fig. 8 shows the accuracy  $\sigma_{x_0-x_c}$  at different power index  $t$  for experimental and simulated electrons at different energies with fixed  $W_0=3$ . Both the experimental and simulated data behave similarly: the trend of the curves show a moderate decrease for small values of  $t$  ( $t < 4$ ) and then gradually level off. One should note that the decrease trend will cease at certain point as the differences of the weight values increase exponentially and the shower core region with higher  $A_{l,c}$  will be overestimated at larger values of  $t$ . Therefore, we will later select  $t=7$  for calculating the shower centre to demonstrate the accuracy of this method.

## 5 Results

### 5.1 Stability of the method

The dead channels and sensors, which are diversely located in the different layers and quadrants, together with the showers which are close to the insensitive or over-sensitive region (e.g. gap and overlap) may lead to a distortion of the transverse hit profile. These effects bring position dependent fluctuations on the shower centre determination. To investigate the stability of the method due to the geometry reasons, a position dependent shower centre reconstruction scan is performed. Fig. 9 shows the residual between the calculated shower centre and the cluster position found in the first layer as a function of primary particles position along  $x$  and  $y$  directions extracted from the simulation. The residual values which are distributed consistently along both directions prove the method is stable.

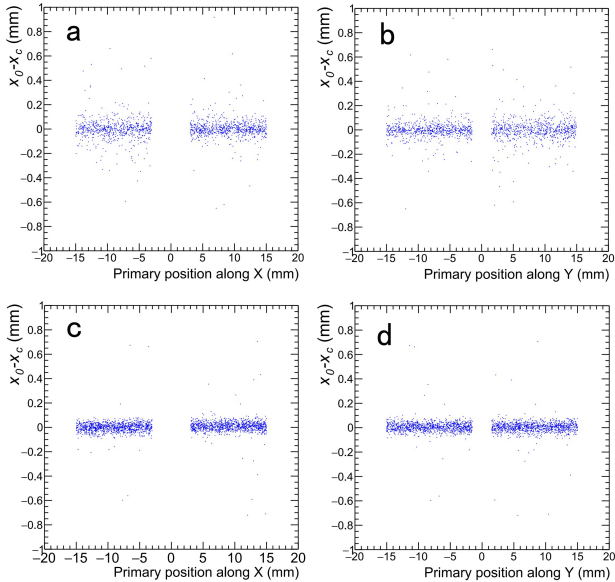


Fig. 9. Residual between reconstructed shower centre  $x_0$  and cluster in the first layer  $x_c$  as a function of primary particle position in  $x$  and  $y$  directions for 5.4 GeV (a, b) and 100 GeV (c, d) in the simulation. The gap and overlap region are not taken into account.

## 5.2 Experimental verification

The accuracy of the shower centre reconstruction is studied by comparing the shower position  $x_c$  to the position  $x_0^\dagger$  of the cluster centre position on the first layer.

The comparison of residual distribution for both experimental data and simulation are shown in Fig. 10. Two energies of electrons, which are 5.4 GeV and 100 GeV, represent the low and the high energy intervals in the data. The distributions are approximately Gaussian and centred around zero. The width of the distribution for experimental is slightly larger than the simulation. A deviation of the centre is visible for the experimental data to the positive side (0.01 mm), which is probably due to the fact that the small inclination of the beam towards to the detector in the experiments is not fully corrected in the analysis. This effect is not present in the simulation as the trajectories of the incident electrons are parallel to the  $z$  axis.

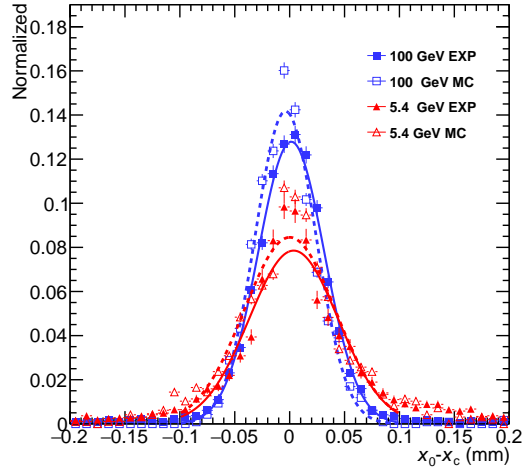


Fig. 10. Distribution of the shower reconstructed position  $x_0$  with respect to the cluster position  $x_c$  in layer 0 for experimental and simulated data.

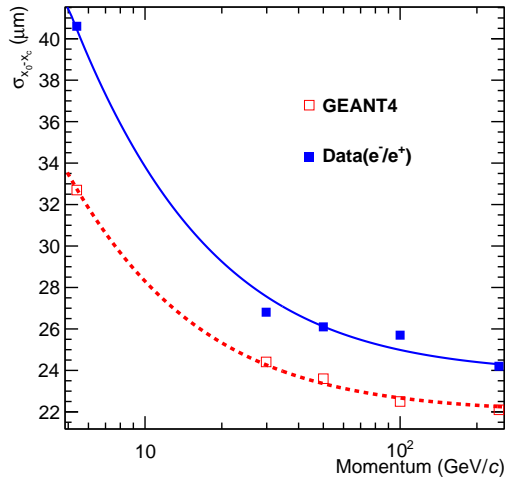


Fig. 11. Width of the distribution of  $(x_0 - x_c)$  as a function of beam momentum for experimental and simulated data.

The obtained accuracy of shower centre reconstruction is represented in Fig. 11 as a function of beam momentum  $p$ . The momentum dependence can be described by Eq.(6).

$$\sigma_x = \alpha \oplus \frac{\beta}{\sqrt{p/\text{GeV}/c}} \quad (6)$$

The parameters  $\alpha$  and  $\beta$  obtained from a fit to the observed distribution are shown in Tab. (5). The accuracy of shower centre reconstruction with FoCal high granularity calorimeter is below 100  $\mu\text{m}$  in a wide range of momenta. For higher momenta (e.g. above 30  $\text{GeV}/c$ ),

<sup>†</sup>Here the focus is put only on the  $x$  coordinate since the  $y$  coordinate behaves similarly.

the precision is less than  $30 \mu\text{m}$ . The results in the simulation is marginally better than the experiment since the limited precision of the alignment in the experimental data slightly degrades the precision.

Table 5. Parameter value of shower centre reconstruction accuracy.

Data source	$\alpha$ ( $\mu\text{m}$ )	$\beta$ ( $\mu\text{m}$ )
experimental	$23.80 \pm 0.36$	$76.01 \pm 1.95$
simulation	$21.95 \pm 0.12$	$56.47 \pm 0.74$

## 6 Conclusion

Benefit from the small Molière radius of tungsten absorber, the extremely high granularity CMOS based digital calorimeter - FoCal enables close photons or electrons separation down to a few millimetres. The digital information provided by the calorimeter requires distinctive method which is different from the conventional gravity centre with energy deposition in the transverse segments. Therefore, an unique method that utilizes the digital information from all the layers together with power law weight to enhance the significance of the shower core region was established and studied in this paper. The pre-

cision of the reconstruct method was verified by comparing simulated and experimental data which covers wide energy range. By optimizing the parameters, the precision of this method can be better than  $30 \mu\text{m}$  in a broad range of energies for not only electrons but also for photons. Moreover, it establishes the basis for the further detailed properties of the three-dimensional distributions of electromagnetic showers and their event-by-event fluctuations.

## 7 Acknowledgements

The author wish to thank prof. dr. T. Peitzmann, dr. G. Nooren, dr. M van Leeuwen, A. van den Brink and dr. N. van der Kolk from Utrecht University for providing the experimental data and for their support. The beam test at DESY in 2014 was supported by the European Community - Research Infrastructure Action under the FP7 “Capacities” Specific Programme, AIDA-C 24 C2018 JINST 13 P01014 DESY-2014-04. This work was supported in part by the China Scholarship Council and the Dutch research organisation NWO-I (formerly FOM).

## References

- 1 E. Shuryak. Physics of strongly coupled quark-gluon plasma. *Progress in Particle and Nuclear Physics*, 62(1):48–101, 2009.
- 2 The ALICE Collaboration. The ALICE experiment at the CERN LHC. *Journal of Instrumentation*, 3(08):S08002, 2008.
- 3 T. Peitzmann and H. Markus. Direct photons from Relativistic Heavy-Ion collisions. *Physics Reports*, 364(3):175–246, 2001.
- 4 I. Andreas et al. Photon polarization as a probe for quark-gluon plasma dynamics. *Physics Letters B*, 666(4):315–319, 2008.
- 5 T. Peitzmann. Measurement of forward direct photon production in p-A at the LHC with ALICE - A probe for nuclear PDFs and saturation. *POS, DIS2016:273*, 2016.
- 6 I. Helenius et al. Probing the small- $x$  nuclear gluon distributions with isolated photons at forward rapidities in p+Pb collisions at the LHC. *Journal of High Energy Physics*, 2014(9):1–18, 2014.
- 7 Harald Fritzsch. Producing heavy quark flavors in hadronic collisions- a test of quantum chromodynamics. *Physics Letters B*, 67(2):217–221, 1977.
- 8 A. Dainese. ALICE potential for heavy-flavour physics. *Journal of Physics G Nuclear Physics*, 34(4):403–410, 2007.
- 9 Alice Collaboration.  $J/\psi$  suppression at forward rapidity in Pb-Pb collisions at  $\sqrt{s_{NN}} = 2.76$  TeV. *Physical Review Letters*, 109(7):–, 2012.
- 10 A. D. Frawley. Cold Nuclear Matter Effects and Heavy Quark Production in PHENIX. *Nuclear Physics A*, s 910-911(8):123–130, 2013.
- 11 T. Price. MAPS Technology for Vertexing, Tracking, and Calorimetry. *Physics Procedia*, 37:932–939, 2012.
- 12 R. Turchetta et al. A monolithic active pixel sensor for charged particle tracking and imaging using standard vlsi cmos technology. *Nuclear Inst and Methods in Physics Research A*, 458(3):677–689, 2001.
- 13 M. Mazouz, L. Ghedira, and E. Voutier. Determination of shower central position in laterally segmented lead-fluoride electromagnetic calorimeters. *Physics*, 455(2):499–501, 2015.
- 14 G. A. Akopdjanov et al. Determination of photon coordinates in a hodoscope cherenkov spectrometer. *Nuclear Instruments and Methods*, 140(3):441–445, 1976.
- 15 L. Bugge. On the determination of shower central positions from lateral samplings. *Nuclear Instruments and Methods in Physics Research*, 242(2):228–236, 1986.
- 16 A. P. De Haas et al. The focal prototype - an extremely fine-grained electromagnetic calorimeter using cmos pixel sensors. *Journal of Instrumentation*, 13(1), 2018.
- 17 A. Brogna. Manual phase1. *IPHC, Strasbourg*.
- 18 S. Agostinelli, J. Allison, K. Amako, J. Apostolakis, H. Araujo, P. Arce, M. Asai, D. Axen, S. Banerjee, and G. Barrand. Geant4-a simulation toolkit. *Nuclear Instruments and Methods in Physics Research*, 506(3):250–303, 2003.
- 19 C. Zhang. Measurements with a high-granularity digital electromagnetic calorimeter, Ph.D. thesis, Utrecht University, 2017.